

Nonlinear Evolution of Kink Unstable Jets, UW-CPTC 11-8

C. S. Carey ^{1,4}, C. R. Sovinec ^{2,4}, and S. Heinz ^{3,4}

ABSTRACT

We investigate the launching and stability of extragalactic jets through nonlinear magnetohydrodynamic (MHD) simulation and linear eigenmode analysis. In the simulations of jet evolution, a small-scale equilibrium magnetic arcade is twisted by a differentially rotating accretion disk. These simulations produce a collimated outflow which is unstable to the current driven $m = 1$ kink mode for low rotational velocities of the accretion disk relative to the Alfvén speed of the coronal plasma. The nonlinear evolution of kink unstable jets is investigated in detail. We find that our choice of initial conditions (uniform mass density and a dipole magnetic field) produces a magnetic tower with a close fitting return magnetic flux and a decreasing magnetic pitch profile. The line-tying effect of the highly conducting accretion disk stabilizes the base of the jet allowing for the formation of a collimated outflow, even though the bulk of the column is unstable. A nonlinear transfer of magnetic energy via the kink mode results in an enhancement of the poloidal magnetic flux at the end of the jet at early times and a large scale helical structure in the bulk of the jet at late times. The results of the jet simulations are compared to several bent blazars via synthetic radio imaging and polarization predictions.

NOTICE: This report was prepared as an account of work sponsored by the United States Government. Neither the United States nor the United States Department of Energy, nor any of their employees, nor any of their contractors, subcontractors, or their employees, makes any warranty, expressed or implied, or assumes any legal liability or responsibility for the accuracy, completeness, or usefulness of any information, apparatus, product or process disclosed or represents that its use would not infringe privately owned rights.

¹Department of Physics, University of Wisconsin, Madison, WI 53706; present address: MIT Lincoln Laboratory, Lexington, MA 02420; christopher.carey@ll.mit.edu

²Department of Engineering Physics, University of Wisconsin, Madison, WI 53706; sovinec@engr.wisc.edu

³Department of Astronomy, University of Wisconsin, Madison, WI 53706; heinzs@astro.wisc.edu

⁴Center for Magnetic Self-Organization in Laboratory and Astrophysical Plasmas, Madison, WI, USA

1. Introduction

Large-scale, highly collimated energetic plasma outflows are observed in some active galactic nuclei (AGN). Many models have been proposed for the formation of these jets (Ferrari 1998), but their launching, collimation, and stability remain open issues. Recent observations indicate that the magnetic field structure in AGN jets is helical in nature (Asada 2005; Gabuzda 2004; Marscher 2008). This suggests that magnetic fields play a strong role in the collimation of AGN jets, as was proposed by Blandford and Payne (Blandford 1982), and that one can use a magnetohydrodynamic (MHD) model to describe their formation and evolution. However, both theory and laboratory experiments show that helical MHD equilibria can be unstable to current-driven kink modes. Understanding the effect of the kink mode on jet morphology is therefore critical to understanding their evolution. Here, we describe a computational MHD study of the evolution of kink unstable jets.

Many of the earlier computational efforts to model extragalactic jets concentrate on two-dimensional MHD models in which the accretion disk is treated as a boundary condition (Romanova 1997; Ouyed 1997; Ustyugova 2000). Even though each of the studies uses a different initial magnetic field, they all observe the formation of a steady outflow. More recent three-dimensional MHD simulations study the stability of the jet far from the galactic nucleus (Nakamura 2001, 2004). These calculations inject flow and torsional Alfvén waves into an MHD equilibrium and show that wiggled structures form in the jet due to the current driven kink mode. Among the three-dimensional simulations of jet evolution conducted to date, those of Moll, Spruit, and Obergaulinger (Moll 2008) cover the largest range of spatial scales. Their efficient use of the grid allows them to extend the simulated jet to lengths that are three orders of magnitude larger than the launching region. They start with a monopole magnetic field and consider jets driven by a Keplerian accretion disk and by a rigidly rotating disk. For both disk boundary conditions, the simulated jet is unstable to the current driven kink.

All of the simulations cited above depend on the presence of an initial ordered magnetic field, which to date has not been observed in the actual systems. Moreover, all of the three-dimensional simulations start with an initial monopole-like field with net magnetic flux through the accretion disk. Such a field cannot be produced by MHD processes in the disk itself since the magnetic flux through the disk is a conserved quantity. A field of this nature must be absorbed into the disk during its formation. Or, a monopole-like jet field can be wound from the inner edge of a disk with zero net flux, as in the relativistic simulations of a black hole by McKinney and Gammie (McKinney 2004).

Another perspective considers jets produced from an initial dipole-like magnetic field with zero net magnetic flux through the accretion disk. It has been proposed that such fields could be produced by an α - Ω dynamo process (Colgate 1998, 2001) in the disk. In previous work, we examine the stability of jets produced from such a field via three-dimensional MHD simulations (Carey 2009b) and find that Coriolis forces from rotation stabilize the jet in some regions of the

parameter space. In this work, we consider regions in the parameter space where the jet is unstable and study its nonlinear evolution. Similar to the two-dimensional results of Ustyugova, et. al. (Ustyugova 2000), we find that this initial condition produces a magnetically accelerated Poynting jet from the inner disk region. For the conditions considered here, the jet has a pitch profile that decreases with radius and is kink unstable (Carey 2009b). The nonlinear evolution results in poloidal flux enhancement at early times and a long wavelength helical structure in the jet at later times. The distortion resulting from nonresonant kink is related to the evolution of the decreasing-pitch cases in the periodic-geometry study of Lery, et. al. (Lery 2000), but our simulated jets are not restricted by a close-fitting wall. The relativistic computations of Mizuno, et. al. investigate the influence of sheared flow profiles and allow greater helical distortion with a more distant wall location (Mizuno 2011). Saturation there involves the profile relaxation effects discussed in Sec. 3.3 below, but we also find line-tying to be important in our non-periodic configuration.

The paper is organized as follows. The model used for the accretion disk/jet system is described in Sec. 2, and the simulation results are presented in Sec. 3. In order to give the reader a broad picture of the simulation results, the general time evolution of the jet is described in Sec. 3.1. Detailed aspects of the simulations are examined in subsequent sections including jet expansion and collimation (Sec. 3.2), jet stability (Sec. 3.3), line-tying effects (Sec. 3.4), and poloidal flux conversion via a nonlinear transfer of energy (Sec. 3.5). In Sec. 3.6, synthetic radio images of the simulated jet are compared to several bent blazars. Conclusions based on these results are offered in Sec. 4.

2. MHD Jet Model

To investigate jet propagation, we model the expansion of a magnetic arcade due to accretion disk rotation using a non-relativistic MHD model which ignores gravitational effects. Similar to previous studies (Romanova 1997; Ouyed 1997; Ustyugova 2000), the accretion disk is treated as a boundary condition on the computational domain. The simulation is initialized with axisymmetric vacuum magnetic field that is tied to the disk and has zero net magnetic flux through the disk. Thus, both ends of all magnetic field lines are anchored to the accretion disk. The differential rotation of the accretion disk, which rotates with a Keplerian velocity profile, injects magnetic helicity and magnetic pressure into the magnetic field, causing it to coil and expand. The coiled magnetic field produces a hoop stress on the plasma that collimates it on the central axis. The effect of jet rotation on the stability of the column is explored by varying the rotation rate of the accretion disk in individual simulations.

We numerically evolve the visco-resistive nonrelativistic MHD equations,

$$\frac{\partial n}{\partial t} + \nabla \cdot (n \mathbf{v}) = -\nabla \cdot D_h \nabla \nabla^2 n \quad (1)$$

$$\frac{\partial \mathbf{B}}{\partial t} = \nabla \times (\mathbf{v} \times \mathbf{B}) - \nabla \times \frac{\eta}{\mu_o} (\nabla \times \mathbf{B}) \quad (2)$$

$$\rho \frac{\partial \mathbf{v}}{\partial t} + \rho (\mathbf{v} \cdot \nabla \mathbf{v}) = \frac{1}{\mu_o} (\nabla \times \mathbf{B}) \times \mathbf{B} - \nabla p + \nabla \cdot \nu \rho \nabla \mathbf{v} \quad (3)$$

$$\frac{n}{\gamma - 1} \left(\frac{\partial k_B T}{\partial t} + (\mathbf{v} \cdot \nabla) k_B T \right) = -\frac{1}{2} p \nabla \cdot \mathbf{v} + \nabla \cdot n K \nabla k_B T \quad (4)$$

where n is the particle density, \mathbf{B} is the magnetic field, \mathbf{v} is the flow velocity, p is the thermal pressure, T is the ion and electron temperature, K is the isotropic thermal diffusivity, ν is the viscosity, η is the resistivity, and γ is the ratio of the specific heats chosen such that $\gamma = 5/3$. The particle density, n , is related to the mass density, ρ , by a factor of the ion mass. The pressure and temperature are related by the ideal gas relation, assuming that the electrons and ions have the same temperature, $p = 2nk_B T$. There is an extra term added to the right hand side of the continuity equation (Eq. 1), given by $-\nabla \cdot D_h \nabla \nabla^2 n$. This hyper-diffusive term is added for numerical smoothing, and the diffusivity coefficient (D_h) is chosen to influence only the smallest spatial scales in the numerical representation. The thermal diffusivity (K) is chosen to be 100 times the electromagnetic diffusivity. The effect of the gravitational force due to the massive galactic central object has been ignored, so gravity does not appear in the momentum equation (Eq. 3).

The MHD equations are evolved in time using the NIMROD code (Sovinec 2004). NIMROD is well benchmarked and has been used to model a wide array of plasma experiments (Sovinec 2003) and magnetospheric physics (Zhu 2006). A cylindrical computational domain with a cylindrical coordinate system given by (r, θ, z) is used. The spatial discretization scheme combines two numerical methods. A mesh of high-order finite elements is used in the poloidal (r - z) plane, where the degree of the polynomial basis functions is chosen at run-time, and the azimuthal (θ) direction is represented with finite Fourier series. The parameter m is used to identify Fourier components in the azimuthal direction. Convergence studies show that a resolution of $0 \leq m \leq 10$, is sufficient for the dynamics of the expanding jet (Carey 2009a). Using logarithmic packing of the poloidal mesh on the central axis and disk boundary, we can resolve the jet dynamics in a large domain using a poloidal mesh of 30 by 100 elements of fifth-degree polynomials.

Previous studies searching for steady state outflows have treated the outer boundaries of the domain with open boundary conditions, allowing kinetic and magnetic energy to flow out of the domain (Romanova 1997; Ouyed 1997; Ustyugova 2000). We use closed, perfectly conducting

boundary conditions on the outer boundaries to avoid inward propagating wave characteristics. While this boundary condition is certainly unphysical, the outer boundaries are placed at distances of $r = 60 r_i$ and $z = 200 r_i$, where r_i is the inner radius of the accretion disk, which is far from the dynamic region of the calculation.

The model of the accretion disk/jet system treats the accretion disk as a boundary condition at $z = 0$, where a smoothed axisymmetric Keplerian velocity profile is applied to v_θ :

$$v_\theta(r, \theta, z = 0) \propto \frac{r}{(r^2 + r_i^2)^{3/4}}. \quad (5)$$

The remaining components of the fluid velocity on the disk boundary at $z = 0$ are chosen such that $v_r = v_z = 0$. A Dirichlet boundary condition is applied on the other, distant boundaries with $\mathbf{v} = 0$. On all of the boundaries, the number density is constrained to be constant. The hyper-diffusive term in Eq. 1 allows mass to diffuse through the disk boundary to fill in the coronal mass that is removed by the jet flow. All of the boundaries are treated as perfect conductors by holding the normal component of the magnetic field constant in time.

The initial condition is a currentless coronal magnetic field, just above the accretion disk. This field is chosen such that there is zero net magnetic flux through the accretion disk boundary. The poloidal magnetic flux, ψ , defined by $\mathbf{B} = \nabla\psi \times \nabla\theta$, is chosen to be

$$\psi(r, z = 0) = r^2 \left[1 + \left(\frac{r}{r_i} \right)^2 \right]^{-\alpha} e^{-r^2/r_o^2} \quad (6)$$

on the disk boundary, where α is a parameter with $0 < \alpha < 1$. The initial magnetic field is found in terms of the magnetic potential, Φ , which satisfies Laplace's equation and is given by

$$\mathbf{B} = \nabla\Phi. \quad (7)$$

An analytic solution for Φ in the domain is found by solving the boundary value problem $\nabla^2\Phi = 0$, where the normal component of $\nabla\Phi$ on the accretion disk boundary is specified by Eq. 6,

$$\frac{\partial\Phi}{\partial z} = \frac{1}{r} \frac{\partial\psi}{\partial r}, \quad (8)$$

and $\Phi = 0$ on all of the other boundaries. The poloidal flux on the disk boundary increases from zero at $r = 0$ to a maximum value at the O-point of the magnetic field, defined to be the radius where $B_z = 0$, and then exponentially decays to zero. For the calculations discussed here, the values $\alpha = 3/4$ and $r_o = 30 r_i$ are used. For this choice of α , the radius of the O-point of the magnetic field is at $15.13 r_i$.

The initial number density and temperature are constant across the computational domain. Thus, the entire domain is initially filled with a plasma that is essentially unmagnetized away from the initial arcade, and the magnetized jet expands into this thermal plasma. The initial flow velocity is set to zero, and the accretion disk flow is ramped from zero at $t = 0$ to a steady profile within one turn of the disk at $r = r_i$. Due to inertial effects, the disk rotation acts to twist the coronal magnetic field, generating an axial $\mathbf{J} \times \mathbf{B}$ force which accelerates flow on the central axis. This twisting of the magnetic field also creates a strong θ -component to the field, causing a hoop stress which pinches the plasma on the central axis and collimates the outflow.

The results discussed here are given in units of the initial field quantities. All velocities are given in units of the Alfvén velocity at the origin, $v_{Ao} = B_o \rho_o^{-1/2}$, where B_o and ρ_o are the magnetic field and mass density at the origin respectively. The magnetic field is given in units of B_o . Time is given in units of T_i , the rotation period of the disk at $r = r_i$.

Four dimensionless parameters are used to describe the system. The first three are commonly used to describe plasma systems: the Lundquist number, $S = \tau_R \tau_{Ao}^{-1}$, where $\tau_R = \mu_o \pi r_i^2 \eta^{-1}$ is the resistive diffusion time across the inner radius of the accretion disk and $\tau_{Ao} = r_i v_{Ao}^{-1}$ is the Alfvénic propagation time across the inner radius of the disk based on the Alfvén speed at the origin; the magnetic Prandtl number, $P_M = \nu \mu_o \eta^{-1}$; and the plasma beta at the origin, $\beta = P_T P_B^{-1}$, where P_T is the thermal pressure and P_B is the magnetic pressure. The last dimensionless parameter, the drive parameter, \hat{V}_D , is defined as

$$\hat{V}_D = \frac{v_\theta(r = r_i, z = 0)}{v_A(r = r_i, z = 0)}, \quad (9)$$

where v_A is the Alfvén velocity. This parameter can be understood as the ratio of how fast the accretion disk twists coronal magnetic field lines to how fast the information of this twisting propagates through the corona. Three sets of parameters are considered: P_M , β , and S are fixed at 1, 1, and 1×10^3 respectively, and \hat{V}_D is varied with the values 0.5, 1.0, and 2.0. The values of \hat{V}_D are chosen to be similar to previous studies (Moll 2008; Nakamura 2004; Ouyed 2003) which consider sub-Alfvénic disk rotation. In our previous work (Carey 2009b), we hold the product $S \cdot \hat{V}_D$ constant as \hat{V}_D is varied between simulations and considered values of $S = 1256.6$, 628.3, and 157.1. In this work, we hold S constant in order to maintain an unstable jet.

3. Jet Simulation Results

3.1. Nonlinear Jet Evolution

We first take a broad view of the nonlinear evolution of the jet in this section, and then examine details such as stability and collimation in later sections. We concentrate on the $\hat{V}_D = 0.5$ case in this section since we are able to run it out to longer times than the higher \hat{V}_D cases. Three-

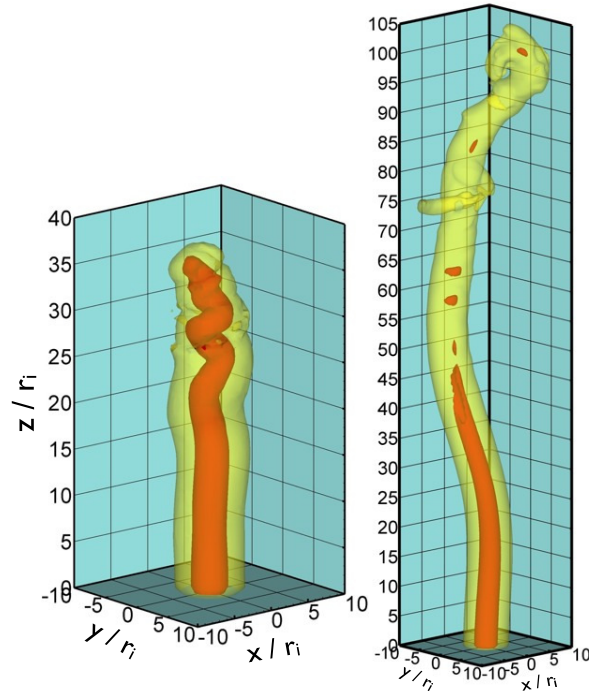


Fig. 1.— Iso-surfaces of $|\vec{B}| = 0.21$ (yellow) and 0.39 (red) in units of $\vec{B}(r = 0, z = 0, t = 0)$ for $\hat{V}_D = 0.5$ at $t = 22.2$ (left) and $103.3 T_i$ (right).

dimensional iso-surfaces of $|\vec{B}|$ are plotted in Fig. 1. The times considered in these plots are after saturation of the kink mode, which occurs at $t \approx 10 T_i$. The effect of the kink on the jet morphology shortly after saturation is clear in the plots in Figs. 1. The kink initially creates a short wavelength helical distortion at the end of the jet. As is discussed in Sec. 3.4, the lower half of the jet remains axisymmetric due to the stabilizing effect of the line-tied disk boundary. As the jet expands, the nonlinear cascade of energy to higher m creates turbulent structure at the end of the jet which breaks up the short wavelength helical structure. At late times in the simulation, a long wavelength helix becomes evident in the jet. As discussed in more detail in Sec. 3.5, this helix is a result of the nonlinear transfer of energy from the $m = 0$ mode to the $m = 1$.

The evolution of the the magnetic topology can be seen in Fig. 2 where magnetic field line traces are plotted at various times. The field lines are colored according to the Alfvén velocity. The effect of the kink mode on the magnetic topology is evident in the $t = 22.15 T_i$ plot where it has tangled the magnetic field lines at the end of the jet. Over time this tangled region propagates axially with the expanding jet, and the field lines below maintain a helical structure. The long wavelength helical structure generated by the kink can be seen at $t = 103.3 T_i$ where a secondary helix is evident in the field line structure.

Our choice for the initial magnetic field and mass density has a significant effect on the magnetic structure which is generated at later times. The magnitude of the initial magnetic field has a

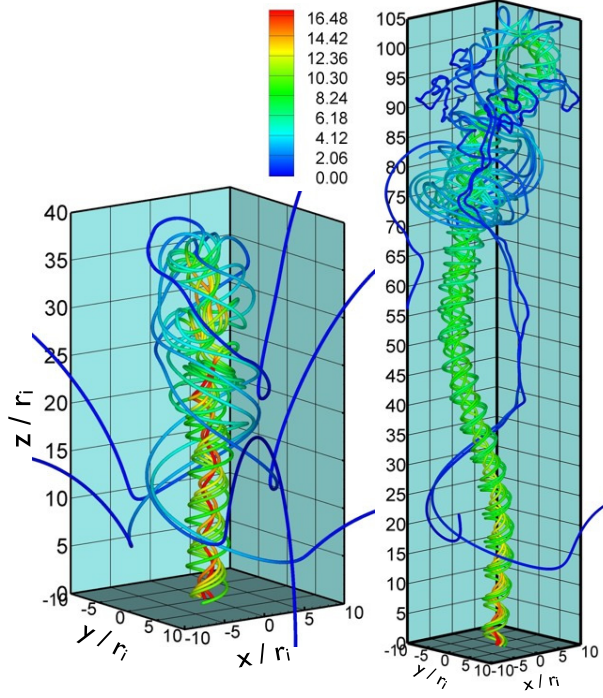


Fig. 2.— Magnetic field lines traces for $\hat{V}_D = 0.5$ at $t = 22.2$ (left) and $103.3 T_i$ (right) starting from the disk boundary at radii: $r = 0.5, 0.8, 1.1, 1.4, 1.7,$ and $2.0 r_i$. Field lines are colored by V_A in units of $V_A(r = 0, z = 0, t = 0)$.

dominant dipole component which scales with the distance from the origin (ζ) as $B \propto \zeta^{-3}$, and the initial number density is uniform. Thus, the initial Alfvén velocity also scales as $V_A \propto \zeta^{-3}$. The information about the twisting of the magnetic field propagates very slowly in regions of small V_A . As can be seen in Fig. 2, this causes the magnetic field lines in the expanding jet to thread through the initial magnetic structure, which is discussed in more detail in Section 3.2. The resulting magnetic structure in the jet is shown in Fig. 3 where radial profiles of B_z and B_θ are plotted for $\hat{V}_D = 0.5$. It should be noted that B_r is not examined in this plot as it is much smaller than the other two components. The magnetic structure in the jet resembles that of the laboratory reversed field pinch (RFP). The RFP is a toroidal plasma confinement scheme which has poloidal and toroidal magnetic field which are comparable in magnitude, and the toroidal field changes sign at what is commonly referred to as the reversal surface. As can be seen in Fig. 3, B_z and B_θ are comparable in the jet, and B_z (which is analogous to the toroidal field in the RFP) changes sign at a reversal radius. The reversal radius is at $r = 4.15$ and at $3.12 r_i$ for $\hat{V}_D = 0.5$ and 1.0 respectively. Thus, the reversal radius decreases with increasing \hat{V}_D . While the magnetic-field distribution in the jet and the RFP are similar, they result from very different processes. The reversal of B_z in the jet is a result of the expanding jet pushing through the initial magnetic structure, while reversal of toroidal field in the RFP is due to modification of the mean field by MHD fluctuations.

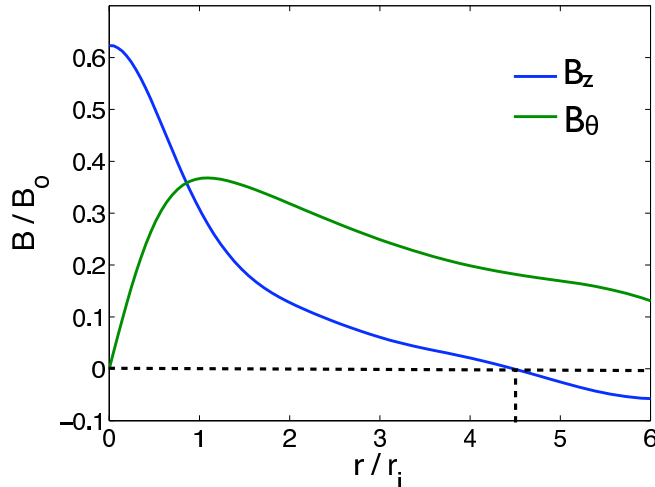


Fig. 3.— Radial profiles of the z and θ components of \vec{B} at $(z, \theta) = (20.0, 0.0) r_i$ for $\hat{V}_D = 0.5$ at $t = 40.98$. The dotted line marks the reversal radius where B_z changes sign.

Our simulated jets have magnetic structures which are similar to that of the laboratory RFP; and thus, a magnetic pitch which is similar to the RFP. Magnetic pitch profiles at various axial positions in the jet for $\hat{V}_D = 0.5$ are plotted in Fig. 4. In contrast, the simulations performed by Moll, Spruit, and Obergaulinger (MSO) (Moll 2008) produce jets with increasing magnetic pitch profiles. Since the disk rotation rates used give comparable values of \hat{V}_D in both simulations (0.5 in our simulations and 0.1 in MSO) we infer that this difference is a result of the different initial conditions used in the simulations. The initial monopole-like magnetic field and mass density in MSO scale with distance from the origin as $B \propto \zeta^{-2}$ and $\rho \propto \zeta^{-3}$ giving an Alfvén velocity which scales as $V_A \propto \zeta^{-1/2}$, while our initial Alfvén velocity scales as $V_A \propto \zeta^{-3}$. Thus, our Alfvén velocity falls off significantly faster than that of MSO. The rotation of the disk launches torsional Alfvén waves into the coronal plasma. These waves essentially cease to propagate relative to the time-scale of the disk rotation at radii where the Alfvén velocity becomes very small. Magnetic field lines at an early time in the jet expansion are plotted in Fig. 5. The field line twist ceases to propagate close to the origin, causing the expanding jet to push through the initial magnetic structure. In contrast, with a slowly decreasing V_A , the field-line twist launched in MSO propagates to distances far from the disk.

3.2. Expansion and Collimation

In this section, we investigate the expansion and collimation of the simulated jets. Similar to the Blandford and Payne model (Blandford 1982), the inertia of the coronal plasma drags on the rotating magnetic field, bending it to generate azimuthal magnetic flux. However, there is not an Alfvén surface inside of which B_θ remains small as in the Blandford and Payne model. As soon as

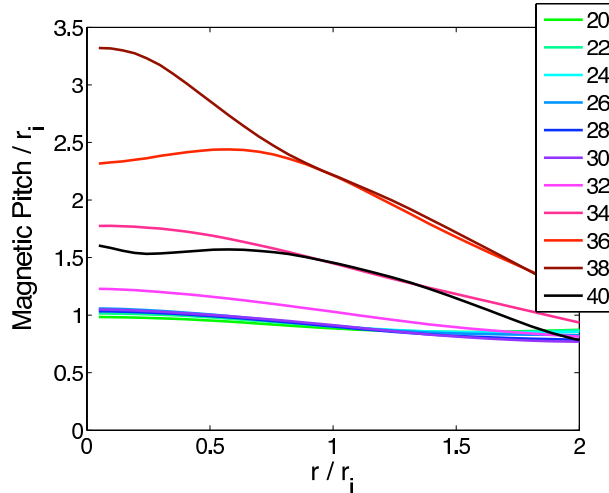


Fig. 4.— Magnetic pitch profiles from the $m = 0$ fields at various axial positions for $\hat{V}_D = 0.5$ at $t = 74.39 T_i$.

the disk rotation starts, B_θ is generated immediately above the accretion disk. The resulting $\vec{J} \times \vec{B}$ forces are plotted in Fig. 6. The current driven by the field line coiling results in a $\vec{J} \times \vec{B}$ force in the axial direction which drives an outflow. This outflow is collimated on the central axis by the $\vec{J} \times \vec{B}$ force in the negative radial direction, often referred to as the hoop stress. The magnetic launching of the outflow is closely related to the magnetic tower model of jet formation and contrasts with the Blandford and Payne model which uses centrifugal acceleration of the plasma to launch the jet.

Short wavelength oscillations are evident in Fig. 6(a). These waves result from the boundary condition $v_z(z = 0) = 0$. The fluid is quickly accelerated to the $\vec{E} \times \vec{B}$ drift velocity above the disk, resulting in a large v_z gradient which, when not fully resolved, launches short-wavelength waves into the plasma. Once a steady state has been reached in the disk boundary layer, these oscillations maintain a constant amplitude. We have examined the resistive power loss due to these oscillations and find it to be small compared to the resistive losses in the disk boundary layer. While undesirable, these steady short-wavelength oscillations do not result in significant energy loss or significantly affect the evolution of larger spatial scales.

The jet is collimated by the hoop stress of the helical magnetic field generated by the disk rotation. The radial forces in the jet at $t = 7.33 T_i$ are presented in Fig. 7, where the magnetic tension force ($-\frac{B_\theta^2}{r}$), the magnetic pressure force ($-\frac{\partial}{\partial r} \frac{B^2}{2\mu_0}$), the centrifugal force ($\frac{v_\theta^2}{r}$), the thermal pressure force ($-\frac{\partial p}{\partial r}$), and the sum of these forces are plotted as a function of radius. The centrifugal and thermal pressure forces are much smaller than the magnetic forces, and the total force is predominately a balance of the outward magnetic pressure against the inward magnetic tension. Discontinuities are evident in the magnetic pressure and thermal pressure forces. These jumps occur at element boundaries, where the finite-element basis functions constrain the field values, but not their derivatives, to be continuous between elements. Examination of p and B^2 indicates

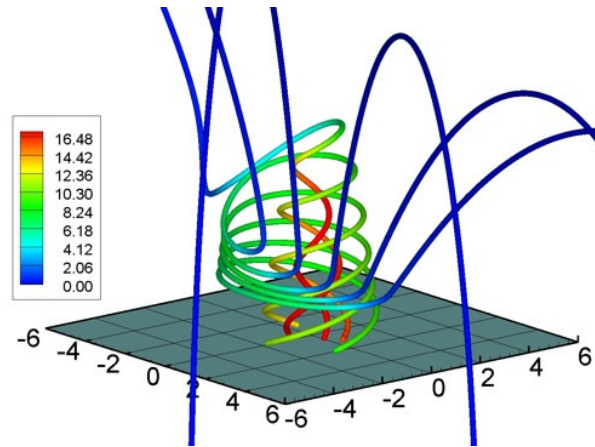


Fig. 5.— Magnetic field lines colored by V_A in units of $V_A(r = 0, z = 0, t = 0)$ at $T = 2.1 T_i$ for $\hat{V}_D = 0.5$.

that the fields themselves are smooth, but truncation error becomes more apparent when we take derivatives of these fields. While the resolution of this region is marginal, the last frame of Fig. 7 shows that the total force in each element is approximately zero, and that the jet is in radial force-balance.

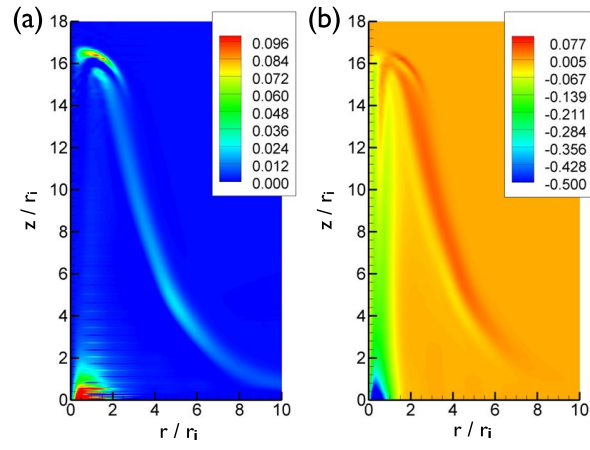


Fig. 6.— Magnetic forces ($\vec{J} \times \vec{B}$) in the z (a) and r (b) directions at $t = 5.45 T_i$ in units of B_o^2/r_i for $\hat{V}_D = 0.5$.

3.3. Stability

Unlike some conditions considered in Ref. (Carey 2009b), the simulated jet is unstable to the $m = 1$ kink mode for the dimensionless parameters considered here. The magnetic energy of the $m = 0, 1, 2,$ and 10 Fourier components is plotted in Fig. 8. The $m = 0$ magnetic energy injected by the disk rotation increases with increasing \hat{V}_D , and more current is driven in the jet. The resulting jet rotation profiles are not sufficient for stabilization, and the kink is more unstable for increasing \hat{V}_D . The average linear growth rates for $4.5 T_i < t < 6.0 T_i$ are $\gamma = 3.41, 4.29,$ and $5.24 T_i^{-1}$ for $\hat{V}_D = 0.5, 1.0,$ and 2.0 respectively. The unstable $m = 1$ mode nonlinearly drives higher- m modes creating a cascade which drives turbulence in the jet. As can be seen in Fig. 8, the increase in the energy of the $m = 10$ mode with increasing \hat{V}_D is larger than that of lower- m modes. Comparing the energy of the $\hat{V}_D = 0.5$ and 1.0 simulations shows that a 26% change in the energy injected into the $m = 0$ mode results in a 52% and 95% change in the energy in the $m = 1$ and 10 modes respectively. Thus, while the growth and saturated energy of the $m = 1$ kink increase with increasing \hat{V}_D , the enhancement of the nonlinear cascade is more significant.

The initial effect of the kink on the jet can be seen in Fig. 9. Here, contours and an isosurface of $|\vec{B}|$ are plotted during the linear phase and after nonlinear saturation for $\hat{V}_D = 0.5$. The kink distorts the axisymmetric jet into a helical structure. This distortion occurs primarily at the end of the jet. Radial profiles of the axisymmetric parallel current ($\lambda = \mathbf{J}_{m=0} \cdot \mathbf{B}_{m=0} / \mathbf{B}_{m=0}^2$) are plotted in Fig. 10 for $\hat{V}_D = 0.5$ during the linear growth of the kink and after saturation. The kink flattens the λ -profile and saturates when λ drops below the critical value for instability.

Our previous work (Carey 2009b) shows that rotation can stabilize jets relative to the ideal kink instability (Carey 2009b). Radial profiles of $\Omega \tau_A$, where Ω is the jet rotation frequency and τ_A is the Alfvén time based on the local on-axis Alfvén velocity, for the $\hat{V}_D = 0.5$ case are plotted in Fig. 11 during the linear growth and after nonlinear saturation of the kink. During the linear phase, $\Omega \tau_A$ is less than the critical stabilizing value calculated in (Carey 2009b) and increases after nonlinear saturation. Thus, we conclude that while jet rotation is likely reducing the growth of the kink, it is not sufficient for full stabilization.

At late times in the simulations the kink mode acts to relax the $m = 0$ current profile at $z \approx 30 r_i$. Axisymmetric parallel current profiles (λ) at $t = 74.39 T_i$ for $\hat{V}_D = 0.5$ are plotted in Fig. 12. The parallel current is peaked for $z \lesssim 30 r_i$ and flattened for $z \gtrsim 30 r_i$. Thus, the column seems to be stable to kink motions for $z \lesssim 30 r_i$ and unstable for $z \gtrsim 30 r_i$. Profiles of $\Omega \tau_A$ at various axial positions are plotted in Fig. 13. Comparison of Fig. 13 with the plots of $\Omega \tau_A$ at earlier times in Fig. 11 shows that over time, the jet rotation increases and eventually has a significant influence on stability for a limited axial range according to the analysis of (Carey 2009b).

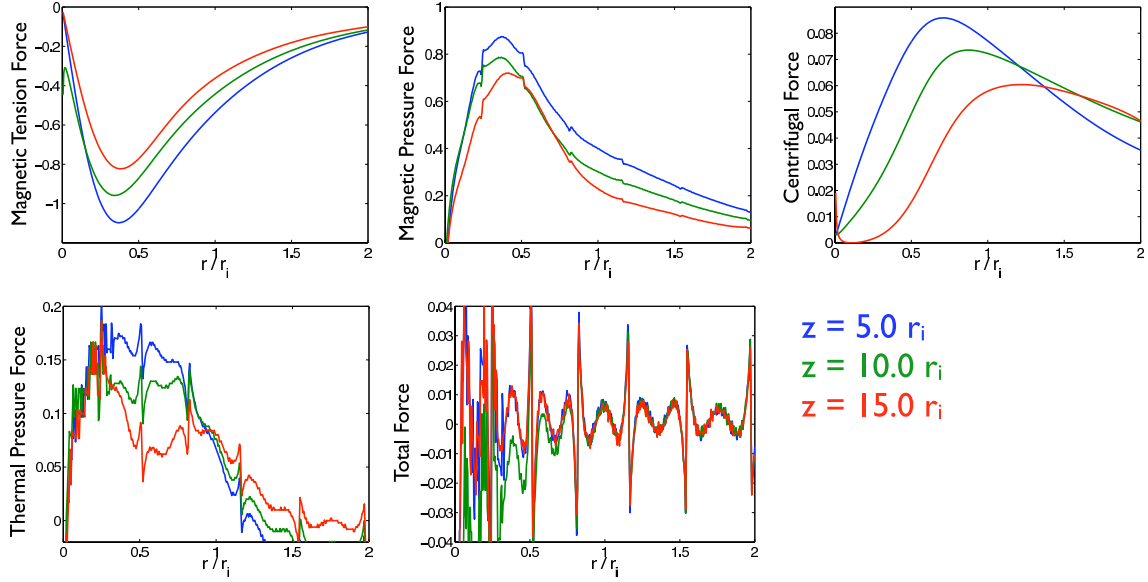


Fig. 7.— Radial components of the MHD forces in the jet as a function of radius for $\hat{V}_D = 0.5$ at $t = 7.33 T_i$ at various axial positions. Forces are given in units of $\frac{1}{r_i} \frac{B^2}{2\mu_o}$. Note that the vertical scales vary between plots.

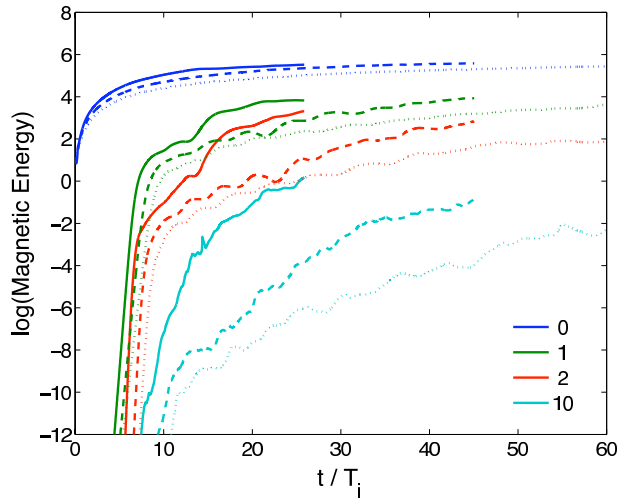


Fig. 8.— Magnetic energy of the $m = 0, 1, 2,$ and 10 Fourier components for $\hat{V}_D = 2.0$ (solid), 1.0 (dashed), and 0.5 (dotted). The magnetic energy is normalized to $V_{dom} B_o^2 / 2\mu_o$, where V_{dom} is the volume of the computational domain.

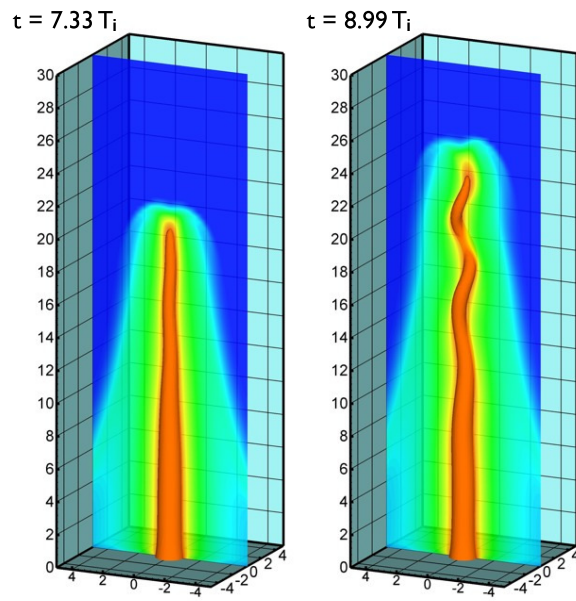


Fig. 9.— Two-dimensional slices and three-dimensional iso-surfaces of $|\vec{B}|$ for $\hat{V}_D = 0.5$ during linear growth of the kink ($t = 7.33 T_i$) and after the kink saturates ($t = 8.99 T_i$).

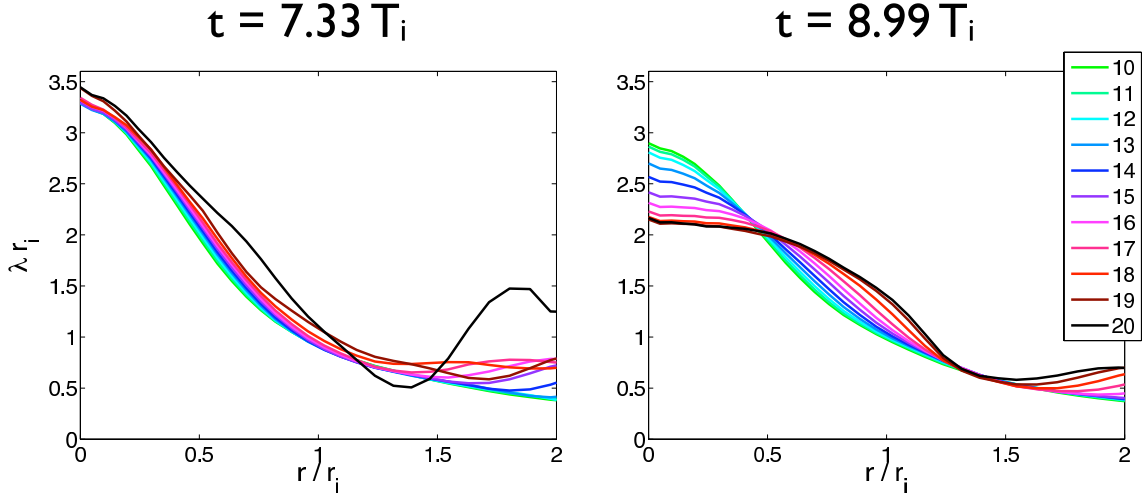


Fig. 10.— Parallel current profiles ($\lambda = \mathbf{J}_{m=0} \cdot \mathbf{B}_{m=0} / B_{m=0}^2$) for $\hat{V}_D = 0.5$ at various axial positions during the linear phase of the kink ($t = 7.33 T_i$) and after the kink saturates ($t = 8.99 T_i$).

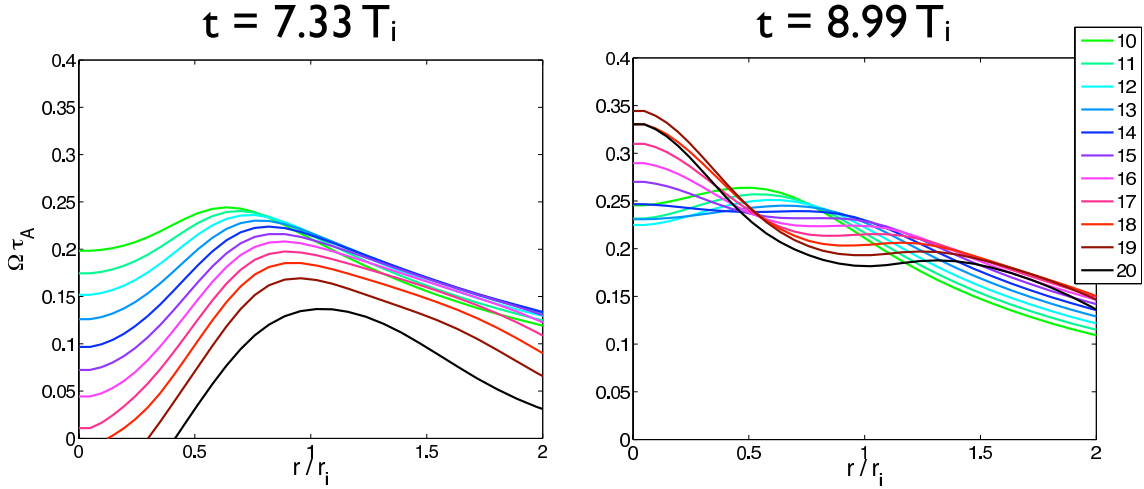


Fig. 11.— Rotation profiles for $\hat{V}_D = 0.5$ at various axial positions during the linear phase of the kink ($t = 7.33 T_i$) and after the kink saturates ($t = 8.99 T_i$).

3.4. Line-Tying Effects

The simulated jet is anchored at one end to the accretion disk by the perfectly conducting boundary condition at $z = 0$, and its propagation front is free to move and is only restricted by the effect of the surrounding plasma. The boundary condition at $z = 0$ prevents unprescribed displacement of the magnetic field lines and is often referred to as a line-tied boundary. The effect of line-tying has been investigated both theoretically (Hegna 2004; Huang 2006; Evstatiev 2006)

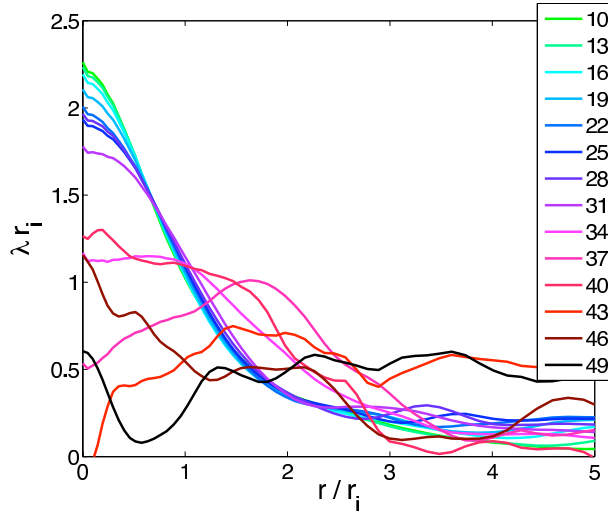


Fig. 12.— Axisymmetric parallel current profiles ($\lambda = \mathbf{J}_{m=0} \cdot \mathbf{B}_{m=0} / B_{m=0}^2$) for $\hat{V}_D = 0.5$ at various axial positions at $t = 74.39 T_i$.

and experimentally (Bergerson 2006; Furno 2007). In general, line-tying is a stabilizing effect. The displacement of the kink must bend magnetic field lines at the boundary, requiring more energy than a periodic configuration. In a periodic cylinder, functions of the form e^{ikz} are eigenfunctions of the MHD equations. Line-tied boundary conditions introduce a dependence on the z -coordinate in the governing equations, and solutions become a superposition of the periodic eigenfunctions (Evstatiev 2006). With line-tying at both ends of a cylindrical plasma, a good rule of thumb is that the system is stable if the Alfvén travel time along the cylinder is less than the inverse growth rate in the periodic system (Huang 2006). We infer that line-tying affects kink growth at positions along the length of the cylinder which communicate with the boundary faster than the growth of the instability.

The effect of line-tying on the stability of the simulated jet is examined in the $\hat{V}_D = 0.5$ simulation. As can be seen in Fig. 9, the kink forms a helical structure in the $|\vec{B}|$ contours for $z \gtrsim 8 r_i$ while the contours for $z \lesssim 8 r_i$ remain nearly uniform in time. This suggests that the magnitude of the $m = 1$ mode is largest in the top half of the jet. This is more evident in Fig. 14 where the $m = 1$ Fourier component of B_x at $t = 8.99 T_i$ is plotted. The mode is clearly dominant in the top half of the jet. As can be seen in Fig. 10, λ is nearly uniform in the z -direction at $t = 7.33 T_i$ before the kink saturates. After saturation (at $t = 8.99 T_i$) the reduction of λ by the kink is most significant at the end of the column. Thus, the energy available to the kink is uniform along the length of the jet, but the unstable $m = 1$ mode and its effect on the $m = 0$ component is most significant in the top half of the column.

The effect of the line-tied boundary condition can be roughly measured by the Alfvénic communication time to the boundary (Huang 2006) plotted in Fig. 15. The Alfvénic communication

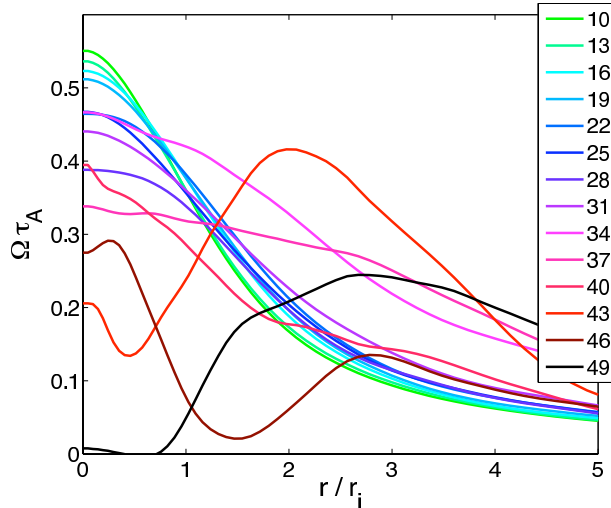


Fig. 13.— Axisymmetric rotation profiles for $\hat{V}_D = 0.5$ at various axial positions at $t = 74.39 T_i$.

time is given by $\tau_A(z) = \int_0^z \frac{1}{v_A(r=0,z')} dz'$ and is calculated numerically using a midpoint rule. The average linear growth rate of the $m = 1$ mode is $\gamma = 3.52 T_i^{-1}$ giving an average growth time of $\gamma^{-1} = 0.284 T_i$. For $z < 7.02 r_i$, the Alfvénic communication time is faster than the $m = 1$ growth time. Thus, we would expect the line-tied boundary to have a stabilizing influence for $z \lesssim 7 r_i$. This agrees well with the $m = 1$ mode structure shown in Fig. 14 which is dominant for $z \gtrsim 8 r_i$.

3.5. Flux Conversion via Nonlinear Energy Transfer

In laboratory experiments, the unstable $m = 1$ kink mode is known to significantly alter the $m = 0$ magnetic field via a process known as magnetic flux conversion in which the kink converts the $m = 0$ toroidal flux to $m = 0$ poloidal flux (Jarboe 1994). In this section, we examine the flux conversion process in the jet simulations with $\hat{V}_D = 0.5$. Contours of the $m = 0$ poloidal magnetic flux are plotted in Fig. 16. As the jet expands, it transports the initial poloidal flux. This is evident at $t = 25.48 T_i$ where the initial poloidal flux has been stretched by the expanding jet. The redistribution of current in the jet due to the kink also alters the poloidal flux. As the kink nonlinearly saturates, the twisting of the current column converts toroidal flux to poloidal flux resulting in a 44% increase in the poloidal flux in the jet at $t = 74.39 T_i$ relative to the maximum poloidal flux at $t = 0$. According to Cowling’s theorem, this flux conversion process requires three-dimensional magnetic perturbations and would not be observed in two-dimensional simulations (Cowling 1934). It should be noted that this process is similar to that which is responsible for spheromak formation in laboratory experiments (Al-Karkhy 1993). However, in laboratory spheromaks the poloidal flux pushes against a conducting flux conserver enhancing the flux conversion, achieving poloidal flux enhancement of hundreds of percent. We surmise that if the simulated jet was to collide with a denser medium, restricting further expansion, the poloidal

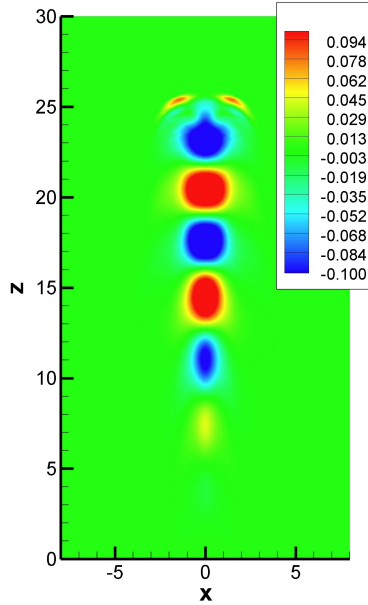


Fig. 14.— Two-dimensional slice of the $m = 1$ Fourier component of \vec{B}_x at $t = 8.99 T_i$ for $\hat{V}_D = 0.5$. The mode is dominant at the end of the column.

flux enhancement would be more significant than that observed here.

We can gain insight into how the MHD fluctuations induced by the kink modify the axisymmetric mean magnetic field by examining the nonlinear transfer of electromagnetic energy in the system. The azimuthal average magnetic energy density in the system is given by

$$\frac{1}{2\mu_o} \langle B^2 \rangle = \frac{1}{2\mu_o} \langle B \rangle^2 + \frac{1}{\mu_o} \sum_{m>0} \vec{B}_m \cdot \vec{B}_m^*, \quad (10)$$

where the angle brackets are used to represent an azimuthal average. The evolution of magnetic energy density is governed by Poynting's theorem for low-frequency dynamics,

$$\frac{\partial}{\partial t} \frac{B^2}{2\mu_o} + \nabla \cdot \vec{S} = -\vec{E} \cdot \vec{J}, \quad (11)$$

where $\vec{S} = \vec{E} \times \vec{B}$ is the Poynting vector which transports electromagnetic energy, and the $-\vec{E} \cdot \vec{J}$ term on the right-hand side acts as an energy source or sink. Taking the azimuthal average of Eq. 11, one finds that the net magnetic energy of each Fourier component also satisfies a Poynting theorem. Thus, the energy of the mean magnetic field obeys

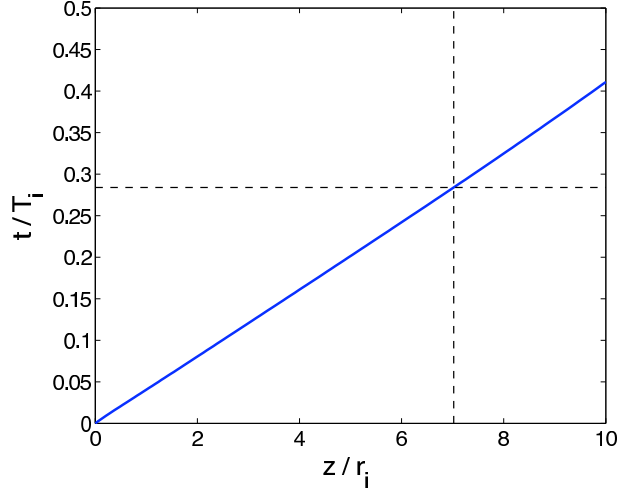


Fig. 15.— Alfvénic communication time to the bottom boundary along the central axis of the jet at $t = 7.33 T_i$ for $\hat{V}_D = 0.5$. The average linear growth time ($0.284 T_i$) of the $m = 1$ mode is indicated by the horizontal dashed line, and the axial position with the corresponding communication time ($7.02 r_i$) is indicated by the vertical dashed line.

$$\frac{\partial \langle B \rangle^2}{\partial t} \frac{1}{2\mu_o} + \nabla \cdot (\langle \vec{E} \rangle \times \langle \vec{B} \rangle) = -\langle \vec{E} \rangle \cdot \langle \vec{J} \rangle. \quad (12)$$

The electric field is given by Ohm’s law, $\vec{E} = -\vec{v} \times \vec{B} + \eta \vec{J}$. Since the ideal term in \vec{E} is a product of two fields, the non-axisymmetric modes ($m \neq 0$) contribute to the mean electric field. Thus, the ideal component of the source term on the right-hand side of Eq. 12 is given by

$$-\langle \vec{E} \rangle \cdot \langle \vec{J} \rangle = 2 \operatorname{Re} \left[\sum_{m>0} \vec{v}_m \times \vec{B}_m^* \right] \cdot \langle \vec{J} \rangle + \langle \vec{v} \rangle \times \langle \vec{B} \rangle \cdot \langle \vec{J} \rangle. \quad (13)$$

It should be noted that the resistive term in Ohm’s Law is proportional to a single field when η is uniform in the θ -direction. Thus, the resistive electric field does not energetically couple different Fourier components in our simulations, but acts as a sink of energy from individual components. Since $\langle \vec{B} \rangle$ is approximately parallel to $\langle \vec{J} \rangle$ behind the propagation front, by examining contributions of individual Fourier components to $\langle \vec{E} \rangle$ parallel to $\langle \vec{B} \rangle$ (known as the MHD dynamo) we can investigate how the higher- m components modify the $m = 0$ magnetic field.

The dynamo action of the non-axisymmetric MHD activity acts to redistribute energy in the jet. Contours of the contribution to the axisymmetric electric field by the non-axisymmetric $m = m'$ component parallel to the $m = 0$ magnetic field ($\langle \vec{E}_{m=m'} \rangle_{\parallel}$) are plotted in Fig. 17 for $m' = 1$ and 2, along with black contours of the $m = 0$ poloidal magnetic flux. In regions where $\langle \vec{E}_{m=m'} \rangle_{\parallel}$ is positive, the $m = m'$ mode removes energy from the axisymmetric magnetic field; and where it is

negative, the $m = m'$ mode deposits energy into the axisymmetric magnetic field. As can be seen in the $t = 49.14 T_i$ plots in Fig. 17, the $m = 1$ mode removes energy from the axisymmetric field on the central axis, and the $m = 2$ mode spreads that energy into the region of enhanced flux at the end of the jet. This nonlinear process which produces the enhanced axisymmetric poloidal flux is similar that which is observed in both laboratory spheromak experiments (Al-Karkhy 1993) and numerical simulations of spheromak formation (Sovinec 2001)

As is discussed in Sec. 3.1, the effect of the kink on the jet morphology changes from creating a short wavelength helical structure at the end of the jet to creating a long wavelength helix in the bulk of the jet. As can be seen in the $t = 74.39 T_i$ plots of Fig. 17, at late times in the jet evolution (well after the kink has saturated) the $m = 1$ mode still removes energy from the $m = 0$ in the region $20 r_i \lesssim z \lesssim 40 r_i$. However, the $m = 2$ does not spread that energy back into the $m = 0$ as it does at earlier times. After the kink saturates, the system becomes a nonlinear damped-driven system in which the $m = 0$ mode drives the $m = 1$. The axial flow transports the $m = 1$ energy away from the region of instability. However, the flow is not sufficient to prevent a buildup of energy in the $m = 1$ component, resulting in the long wavelength helix which is evident in the $t = 74.39 T_i$ plot in Fig. 1.

3.6. Synthetic radio imaging and polarization predictions

We can follow a similar approach to other studies in taking the large scale propagation of our jet and consider it scale free (neglecting the conditions near the disk boundary). In this sense, we consider the jet far away from the disk to be ballistic. We are then free to choose an appropriate scale to compare our numerical results to actual observations of AGN jets.

It is worth noting, however, that the simulation scale is not far from observations of typical AGN jet sources. In fact, the best cases (e.g., M87) are well resolved down to scales reflected in our simulations. Our simulations span a length scale of about 100 inner jet radii r_i . If we take the typical injection scale for a relativistic jet to be of the order of 10 inner disk radii, our characteristic scale r_i corresponds to a physical scale of 60 gravitational radii

$$r_i \sim 60r_g = 60 \frac{GM}{c^2} = 9 \times 10^{14} \text{ cm} M_8 \quad (14)$$

and the outer scale of our simulation would be of order $10^{17} \text{ cm} M_8$ where M_8 is the black hole mass in units of $10^8 M_\odot$. Such scales are well resolved for a number of nearby black holes.

In order to connect the simulations to observations, we calculate the synchrotron emission expected from the simulated jets. We are interested in two observational predictions: the morphology of the synchrotron surface brightness and the polarization signature of jets subject to kink instability.

We consider only the optically thin limit with a particle spectral index of 2.5 such that $N(\gamma) \propto \gamma^{-2.5}$, resulting in a spectral index of $\alpha = 0.75$. We neglect all effects of radiative transfer and, given the near uniform pressure inside the grid, we assume that the spatial distribution of relativistic particles is roughly uniform. In this sense, the synthetic synchrotron maps reflect primarily the evolving structure of the magnetic field in the jet. We treat the relativistic plasma as a dynamically unimportant tracer, neglecting the energy lost to radiation in the actual dynamical evolution (this is appropriate given typical spectral indices observed in AGN jets). Using these assumptions, the total observed intensity along a line of sight $\mathbf{e}_{x'}$ is given by (Konigl 1985)

$$I(y', z') = C \int N (B_{y'}^2 + B_{z'}^2)^{(1+\alpha)/2} dx', \quad (15)$$

where $\mathbf{e}_{y'}$ and $\mathbf{e}_{z'}$ are orthogonal directions in the plane orthogonal to the line-of-sight $\mathbf{e}_{x'}$, and C is composed of constants which give the proper units. The radiation polarization can be found using the Stokes parameters Q and U given by

$$Q(y', z') = C \int N (B_{y'}^2 + B_{z'}^2)^{(1+\alpha)/2} p \cos(2\chi) dx', \quad (16)$$

and

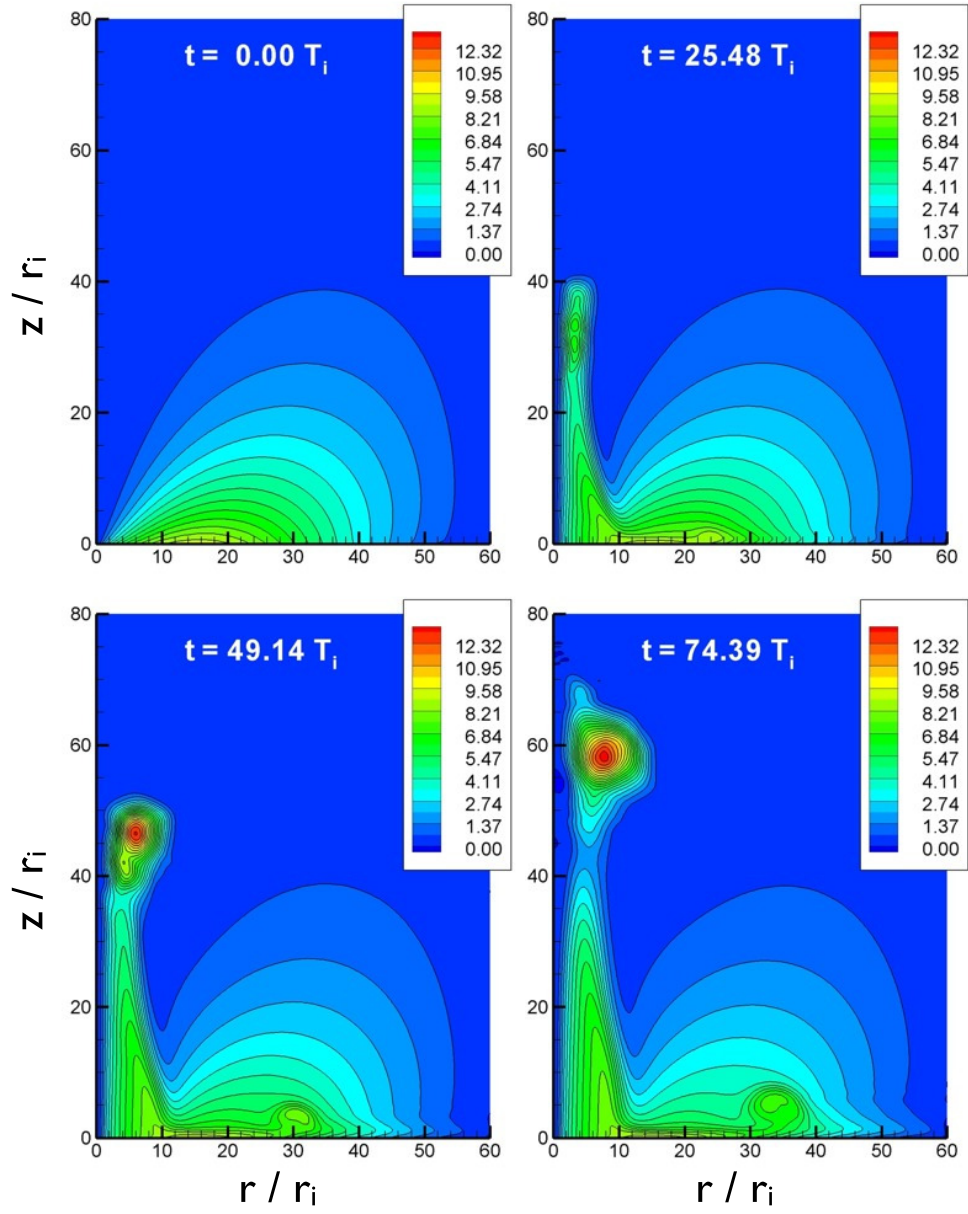


Fig. 16.— $m = 0$ poloidal magnetic flux for the $\hat{V}_D = 0.5$ simulation.

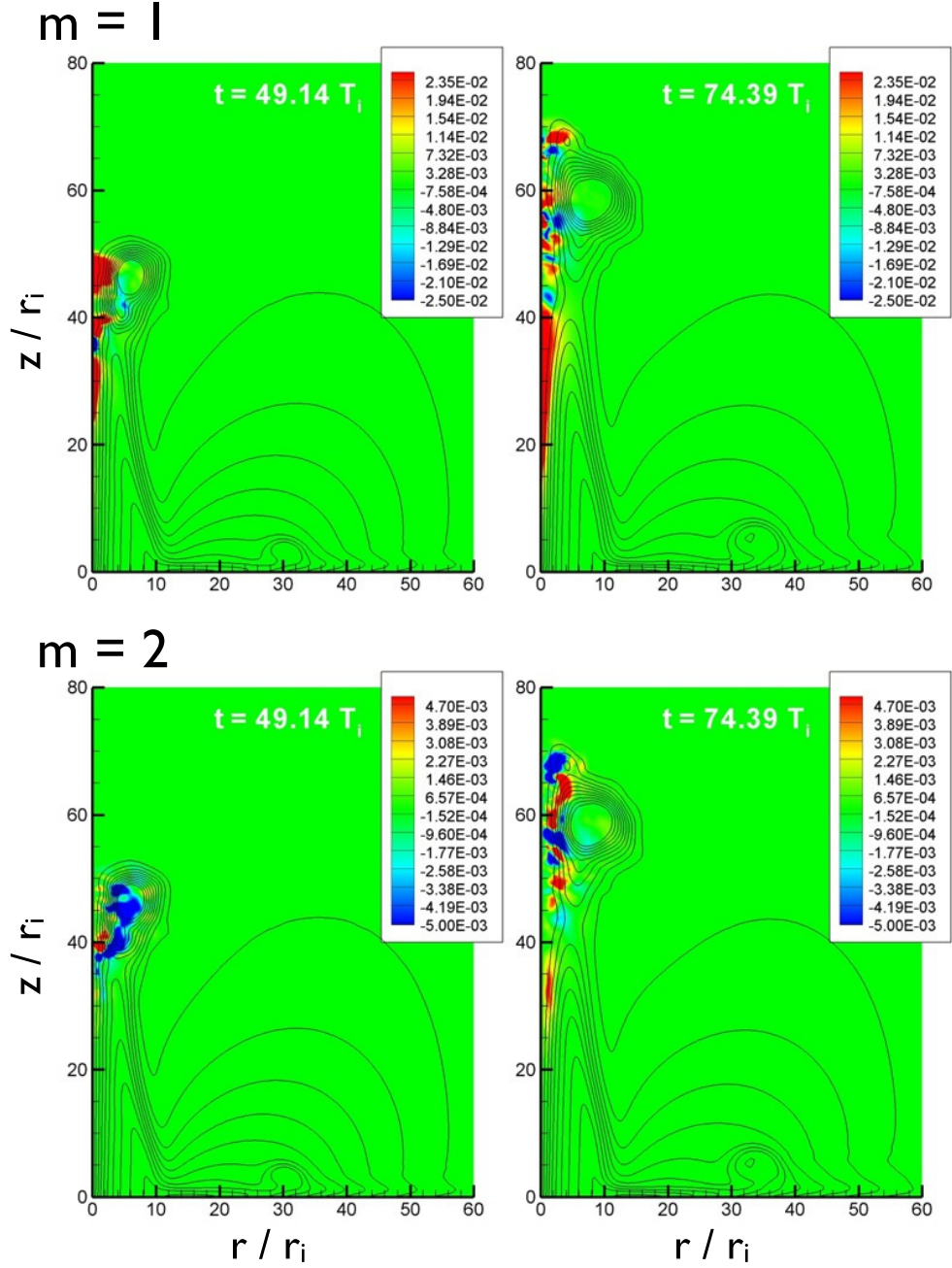


Fig. 17.— Color contours of the $m = 1$ and $m = 2$ MHD dynamos $\left(2 Re \left[\langle -\vec{v}_m \times \vec{B}_m^* \rangle \right] \cdot \frac{\langle \vec{B} \rangle}{\langle |\vec{B}| \rangle} \right)$ in units of $\vec{v}(r = r_i, z = 0) \times \vec{B}(r = r_i, z = 0)$ and black contours of the $m = 0$ poloidal magnetic flux for $\hat{V}_D = 0.5$.

$$U(y', z') = C \int N (B_{y'}^2 + B_{z'}^2)^{(1+\alpha)/2} p \sin(2\chi) dx', \quad (17)$$

where

$$\chi = \arctan \left(\frac{B_{y'}}{B_{z'}} \right) \quad (18)$$

and the intrinsic degree of polarization (p) for a locally uniform magnetic field is

$$p = \frac{3\alpha + 3}{3\alpha + 5}. \quad (19)$$

In terms of the Stokes parameters, the degree of linear polarization (P) is given by

$$P(y', z') = \frac{\sqrt{Q^2 + U^2}}{I}, \quad (20)$$

and the position angle of the mean electric field vector (ξ) is given by

$$\xi(y', z') = \frac{1}{2} \arctan \left(\frac{U}{Q} \right). \quad (21)$$

Contours of the total synchrotron intensity based on the $\hat{V}_D = 0.5$ simulation are shown in Fig. 18 for various observation angles relative to the initial jet axis. The helical structure generated by the kink shows a bend in the observed intensity, and it appears to increase as the observation angle relative to the jet axis decreases. The projected magnetic field vectors as interpreted from the radiation polarization are shown in Fig. 19. The projected magnetic field vectors are found by rotating the projected electric field vector 90° and are represented with lines with lengths which are proportional to $I \cdot P$. There is a clear rotation in the projected magnetic field vectors across the width of the jet. The jet is collimated by a helical magnetic field and as the kink bends the column and shifts it off the central axis, this helix is stretched on the outside and compressed on the inside. This effect combined with the viewing angle results in rotation of the polarization vectors.

3.7. Comparison to observations of bent jets

Because of foreshortening, jet bending is best observed in sources that are oriented along the line of sight. Naturally, these sources will be most Doppler boosted and thus typically found in samples of blazars and BL Lac objects. Indeed, many blazars show evidence of strong bends. In the spirit of the discussion in section 3, these bends can be readily interpreted as the result of the non-linear evolution of kink-unstable jets.

As test cases for comparison, we selected two possible examples of jets showing clear bending from the MOJAVE database, the blazars J1308+326 and J1150+812. Contours are shown in Figs. 20 and 21. Both jets show clear evidence of jet bending.

Both images have a plate scale of roughly 8 pc per mas, indicating that the observations are resolved in scales of roughly 40 pc or 10^{20} cm. While the viewing angle of these sources is unknown, the observed limits on the velocity of $v_{\text{app}} \sim 27c$ and $v_{\text{app}} \sim 7c$ for 1308 and 1150, respectively, implies viewing angles of $\theta \lesssim 2^\circ$ and $\theta \lesssim 8^\circ$, respectively, with corresponding de-projected jet length scales of $l \sim 3$ kpc and $l \sim 1$ kpc, respectively.

Taking the observed scales to correspond to the largest simulated scales (i.e., neglecting the inner boundary condition and regarding the jet as propagating freely into the surrounding medium), we can now compare the observed bending and polarization signatures to the synthetic synchrotron maps shown in Figs. 18 and 19. Similar to the magnetic field vectors in the simulated jet, the magnetic field polarization in 1150+812 is perpendicular to the jet tail on the outside of the bend and rotates nearly 90° across the diameter of the jet. Based on the simulation results, we surmise that this rotation of the polarization vectors could arise from a distortion of the collimating helical magnetic field. Moreover, the bend in the intensity contours of both J1308+326 and J1150+812 compares qualitatively well with that of the synthetic synchrotron intensity of the simulated jet. Thus, we postulate that the bends observed in some jets could be a result of the current driven kink instability.

4. Conclusions

In comparison with the results of Moll et al. (Moll 2008), we note that the initial profiles have a large influence on our simulated jets. With zero net magnetic flux through the accretion disk, the rapidly decreasing Alfvén velocity inhibits the propagation of the torsional Alfvén waves launched by the disk rotation, forcing the jet to expand through the initial magnetic arcade. This results in a magnetic tower with a RFP-like magnetic profile with decreasing magnetic pitch and reversal of the axial magnetic field. Prior to the development of long wavelength distortion, the expanding configuration with distorted end bears some resemblance to the simulated magnetic towers of Nakamura, et. al. that are driven by a volumetric source near the center of a stratified background (Nakamura 2007).

Even when kink unstable, our simulated jets maintain a large degree of collimation. A key reason for this is the line-tied boundary at the accretion disk. The magnetic field lines are anchored to the highly conducting disk requiring more energy for displacement of the column by the kink. This stabilizes the base of the jet, allowing for the formation of the column; and without it, the kink would likely destroy the jet before a collimated outflow could form. Further from the disk, the kink relaxes the collimation of the jet and nonlinearly saturates when the $m = 0$ current is sufficiently flattened. After saturation, the jet is a damped driven system in which the $m = 0$ component drives the $m = 1$, resulting in a large scale helical distortion of the column. Calculations of the line-integrated synchrotron intensity from the kinked jet show that this helix appears as a bend in the jet.

The rotation of the accretion disk generates toroidal magnetic field in the jet. The deformation of the column by the unstable kink mode results in a conversion of this toroidal field to poloidal field. The energy analysis discussed in Sec. 3.5 shows that the $m = 1$ kink removes energy from the $m = 0$ magnetic field on the central axis of the jet and nonlinearly transfers the energy back into the $m = 0$ field at a larger radius resulting in poloidal flux enhancement. Without this flux conversion process, the magnetic energy injected by the disk rotation would be constrained to remain in the jet. The toroidal field injected by the rotation generates a current which leaves the disk at small radii and returns to the disk at larger radii. This closed circuit would prevent the jet from shedding magnetic flux. However, once the toroidal field is converted to poloidal field it is no longer electrically tied to the disk and can be lost from the jet via reconnection processes. Such a shedding of magnetic energy would help to populate the intergalactic medium with magnetic field (Colgate 2001).

5. Acknowledgements

This work is supported by the U.S. Department of Energy Computational Science Graduate Fellowship (DE-FG02-97ER25308) and the National Science Foundation Center for Magnetic Self-Organization in Laboratory and Astrophysical Plasmas (PHY 0821899). Nonlinear simulations were

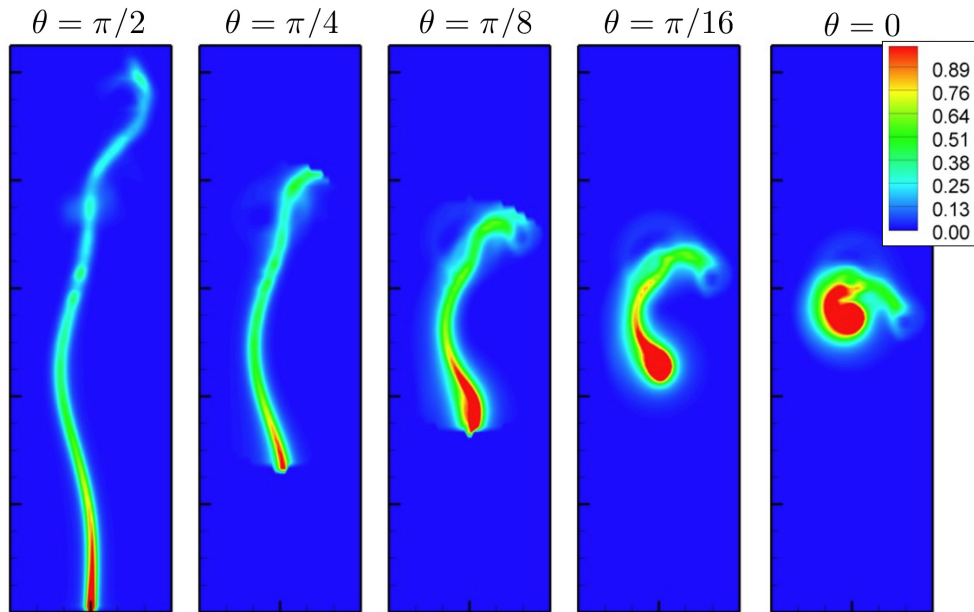


Fig. 18.— Synchrotron intensity at various angles relative to the z -axis (θ) at $t = 103.3 T_i$. The contour levels are consistent between the plots, and the units are arbitrary.

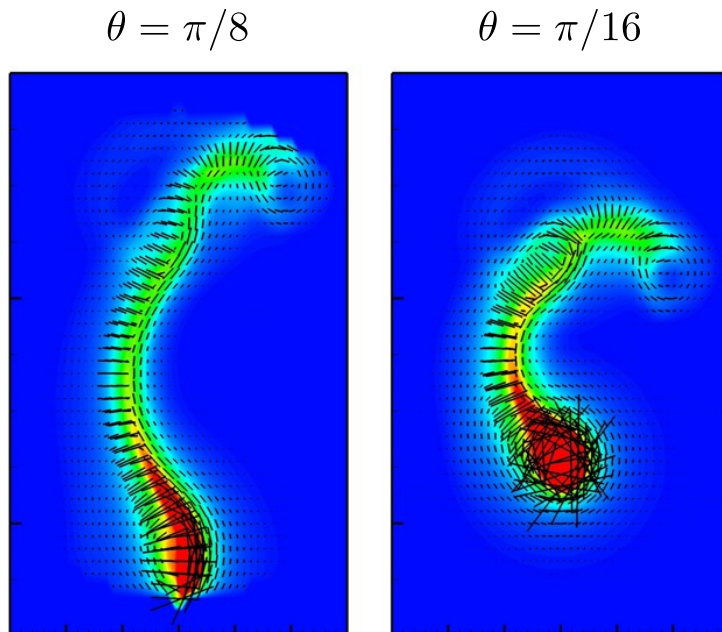


Fig. 19.— Vectors of projected magnetic field vectors and contours of synchrotron intensity at various angles relative to the z -axis (θ) at $t = 103.3 T_i$. The contour levels are consistent between the plots, and the units are arbitrary.

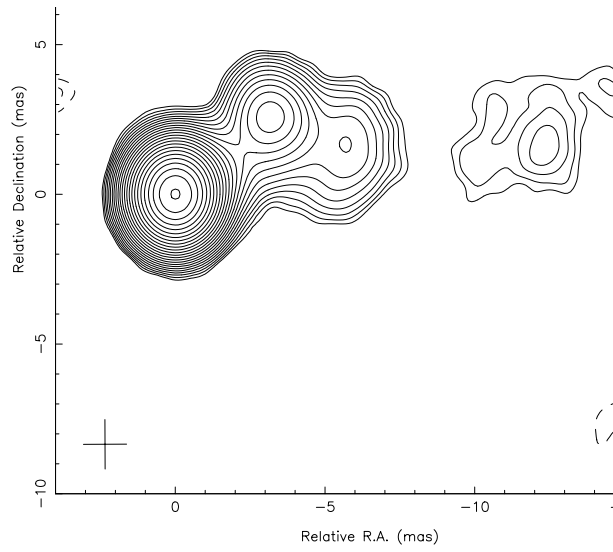


Fig. 20.— Total intensity contours of the blazar 1308+326. (8.03 pc/mas)

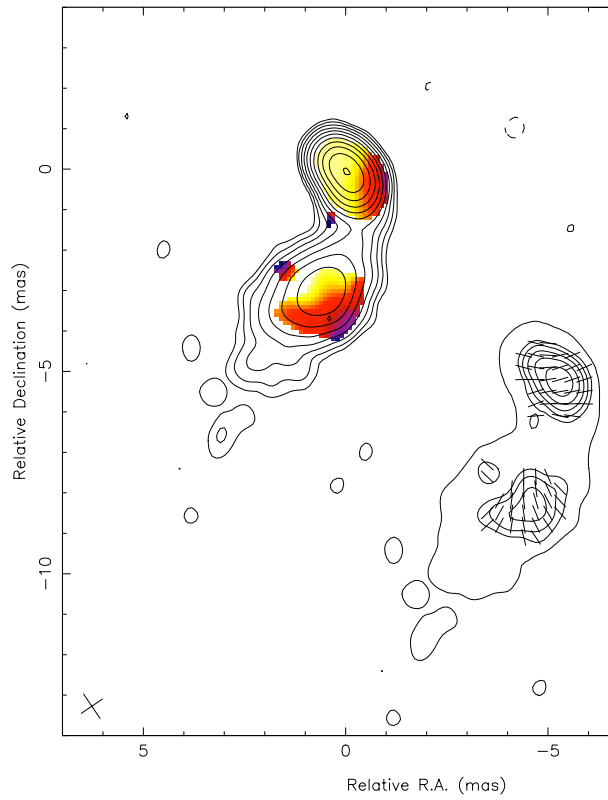


Fig. 21.— Total intensity contours with magnetic polarization vectors of the blazar 1150+812.

performed at the National Energy Research Scientific Computing Center, which is supported by the Office of Science of the U.S. Department of Energy under Contract No. DE-AC02-05CH11231. This research has made use of data from the MOJAVE database that is maintained by the MOJAVE team (Lister et al., 2009, *AJ*, 137, 3718).

REFERENCES

- Al-Karkhy, A., Browning P., Cunningham, G., & Gee, S. 1993, *Physical Review Letters*, 70, 1814
- Asada, K., Inoue, M., Kameno, S., & Nagai, H. 2005, in *ASP Conf. Ser.* 340, *Future Directions in High Resolution Astronomy: The 10th Anniversary of the VLBA*, ed. J. D. Romney, & M. J. Reid (San Francisco: ASP), 168
- Bergerson, W., Forest, C., Fiksel, G., & Hannum, D., 2006, *Physical Review Letters*, 96, 015004
- Blandford, R., & Payne, D. 1982, *MNRAS*, 199, 883
- Carey, C.S. 2009, *A Numerical Study of Magnetohydrodynamic Jet Collimation and Stability* (University of Wisconsin-Madison)
- Carey, C.S., & Sovinec, C.R. 2009, *ApJ*, 699, 362
- Colgate, S., & Li, H. 1998, *Ap&SS*, 264, 357
- Colgate, S., Li, H., & Pariev, V. 2001, *Physics of Plasmas*, 8, 2425
- Cowling, T. 1034, *MNRAS*, 94, 39
- Evstatiev, E., Delzanno, G., & Finn, J. 2006, *Physics of Plasmas*, 13, 072902
- Ferrari, A. 1998, *ARA&A*, 36, 539
- Furno, I., Intrator, T., Lapenta, G., Dorf, L., & Abbate, S. 2007, *Physics of Plasmas*, 14, 022103
- Gabuzda, D., Murray, É., & Cronin, P. 2004, *MNRAS*, 351, L89
- Gardner, F., & Whiteoak, J. 1966, *ARA&A*
- Hegna, C. 2004, *Physics of Plasmas*, 11, 4230
- Huang, Y., Zweibel, E., & Sovinec, C. 2006, *Physics of Plasmas*, 13, 0921202
- Jarboe, T.R. 1994, *Plasma Physics and Controlled Fusion*, 36, 945
- Konigl, A., & Choudhuri, A.R. 1985, *ApJ*, 289, 173
- Lery, T., Baty, H., & Appl, S. 2000, *A&A*, 355, 1201

- Lister, M., MOJAVE Survey, <http://www.physics.purdue.edu/MOJAVE>
- Marscher, A., Jorstad, S., D'Arcangelo, F., & Smith, P. 2008, *Nature*, 452, 966
- McKinney, J., & Gammie, C. 2004, *ApJ*, 611, 977
- Mizuno, Y., Hardee, P., & Nishikawa, K.-I. 2011, *ApJ*, 734, 1
- Moll, R., Spruit, H.C., & Obergaulinger, M. 2008, *A&A*, 492, 621
- Nakamura, M., Uchida, Y., & Hirose, S. 2001, *New Astronomy*, 6, 61
- Nakamura, M., & Meier, D. 2004, *ApJ*, 617, 123
- Nakamura, M., Li, H., & Li, S. 2007, *ApJ*, 656, 721
- Ouyed, R., Clarke, D., & Pudritz, R. 2003, *ApJ*, 582, 292
- Ouyed, R., & Pudritz, R. 1997, *ApJ*, 482, 712
- Romanova, M., Ustyugova, G., Koldoba, A., & et. al. 1997, *ApJ*, 482, 708
- Sovinec, C., Finn, J., & del-Castillo-Negrete, D. 2001, *Physics of Plasmas*, 8, 475
- Sovinec, C., Gianakon, T., Held, E., & Kruger, S. 2003, *Physics of Plasmas*, 10, 1727
- Sovinec, C., Glasser, A., Gianakon, T., Barnes, D., Nebel, R., Kruger, S., Schnack, D., & Plimpton, S. 2004, *Journal of Computational Physics*, 195, 355
- Ustyugova, G., Lovelace, R., Romanova, M., Li, H., & et. al. 2000, *ApJ*, 541, L21
- Zhu, P., Hegna, C., & Sovinec C. 2006, *Physics of Plasmas*, 13, 102307